What can chemical bonding tell us about photoinduced self-healing reactions in inorganic semiconductors? Insight from Bismuth-Antimony Selenide

Anchal Vashishtha[1], Subila Kurukkal Balakrishnan[2], Yaniv Dror[1†], Jitendra Kumar[4], Priyakumari Chakkingal Parambil[4], Eran Edri[1,5*]

[1]Department of Chemical Engineering, Ben-Gurion University of the Negev, Be'er-Sheva 8410501, Israel.

[2]School of Chemical Sciences, Mahatma Gandhi University, Kottayam, 686560, India

[3]Department of Chemical Sciences, Indian Institute of Science Education and Research, Mohali, 140306, India

[4]Department of Electronics Engineering, Indian Institute of Technology, Dhanbad, 826004, India

[5]Ilse Katz Institute for Nanoscale Science and Technology, Be'er-Sheva 8410501, Israel

[†]Current Address: Apollo Solar, Yokneam Illit, 2066722, Israel

*Corresponding author email: edrier@bgu.ac.il

Abstract

Photo-reactive self-healing semiconductors with suitable bandgaps for solar energy conversion offer an intriguing path to making resilient and low-cost photovoltaic devices through the introduction of a self-recovery path. However, only few inorganic photovoltaic materials have such quality, and the underlying chemical properties that enable it are unknown, which poses a significant limit to our ability to study and discover new self-healing semiconductors. Recently, we have found antimony trichalcogenide (Sb_2Se_3, Sb_2S_3) and chalcohalides (e.g., SbSeI) can undergo a reversible photo-induced phase transition (PIPT) in which the structure is restored after photo-induced damage is incurred to the materials. This group of materials offer a unique opportunity for studying PIPT and its limits. In particular, this group of materials facilitates the study of functional permutation to specific crystalline sites, and to finding the limits of PIPT occurrence, which sheds light on the origin of the PIPT and self-recovery of this class of materials. We found that PIPT magnitude decays upon gradual $Bi_{Sb(1)}$ substitution in a $Sb_{2-x}Bi_xSe_3$ homologous series, until nearly one in five Sb ions is substituted with Bi. Then, PIPT diminishes completely. The homologous series occurs along a transition from a covalent to metavalent chemical bonding. By expanding our search, we find a correlation between bonding type and photoreactivity does exist but is an insufficient condition. Instead we suggest that sufficient bonding states at the bottom of the conduction band are also required. This study pushes the limits of designing self-healing inorganic semiconductors for various applications and provides tools to further expansion.

Introduction.

Inorganic semiconductors are integral to the advancement of electronic and energy devices. Yet, their susceptibility to degradation over time presents significant challenges, necessitating innovative approaches to enhance device resilience and sustainability. Traditionally, enhancing material stability has been the primary strategy to impart resilience. Recent research has highlighted the potential of leveraging inherent or induced chemical dynamics to enable self-healing capabilities in inorganic semiconductors.[1]

Drawing inspiration from biological systems, in which organisms naturally repair damage, the concept of self-repairing/healing in materials science refers to a material's ability to autonomously mend defects during its operational life. Self-repair has been extensively explored in organic soft matter and, to a lesser extent, in metals and selected ceramics.[2–9] A relatively mature understanding of this domain is based on the flexible and dynamic nature of metals and organic molecules. However, conventional inorganic semiconductors have a very different landscape, owing to their rigid and crystalline nature. As a result, it is difficult for these materials to self-repair and heal, and literature on self-healing in inorganic semiconductors is scarce. Nonetheless, in recent years, there has been rejuvenated interest in self-healing in semiconductors that can be partly attributed to discoveries in halide perovskites (HaPs).[10–17] These materials, known for their optoelectronic properties and use, have demonstrated intriguing defect dynamics that lead to the ability to self-heal various defects.[18–20] However, owing to the small number of available examples of self-healing semiconductors, finding common chemical features and connecting composition/structure and self-healing remains challenging. Furthermore, finding new mechanisms for self-healing has been elusive.

Solar cell devices exhibit photoinduced chemical dynamics that can lead to self-recovery in their structure or photovoltaic response.[21–23] Investigations have spanned various materials, including silicon, hydrogenated amorphous silicon, transition metal dichalcogenides, and halide perovskites (HaPs), and more recently, main group metal chalcogenides.[24–36] Notably, materials such as germanium diselenide ($GeSe_2$)[33,34] and arsenic trisulphide (As_2S_3)[27,36] have demonstrated reversible photo-induced phase transitions (PIPT) from glassy to crystalline structures. The ability of these materials to revert to their original structure and photoelectronic properties post-stimulus underscores the importance of PIPT in self-healing processes.

Ceratti et al. have made significant contributions to our understanding of self-healing in semiconductors, particularly through their studies on photoluminescence bleach recovery in $APbBr_3$ single crystals (A = CH_3NH^{3+}, methylammonium (MA); $HC(NH_2)^{2+}$, formamidinium (FA); and cesium, Cs^+).[19,37] By employing two-photon microscopy, they induced damage within the crystals and observed the recovery process, revealing distinct behaviors among different perovskite compositions. Their

findings suggest a mechanism involving polybromide species, enhancing our understanding of reversible photobleaching in HaPs. Further, their research distinguished between surface and bulk degradation and healing processes, supported by density functional theory (DFT) simulations, highlighting the role of various cations and the Br_3^- defect in passivation.

Despite these advances, our grasp of the chemical mechanisms underlying PIPT remains incomplete. The scarcity of semiconductors known to undergo reversible PIPT limits our ability to fully exploit this phenomenon for self-healing purposes. Not all materials exhibit PIPT, prompting a need for delineation between those that do and those that do not, which is crucial for guiding the search for new PIPT-capable and self-healing semiconductors.

A recent discovery in the field of quasi-one-dimensional antimony-based semiconductors, such as SbChI and Sb_2Ch_3, where Ch represents selenium or sulfur, has expanded our possibilities.[35] These antimony-based chalcogenides and chalcohalides offer a promising avenue for further research, given their tunable composition and preservation of crystal symmetry, which facilitates the exploration of chemical bonding's impact on PIPT. These materials are not only potent light absorbers but have also shown notable photovoltaic performance, achieving a record power conversion efficiency of 10.5%.[38–40]

This paper examines how novel concepts of chemical bonding correlate with the propensity of materials to undergo PIPT. By analyzing PIPT characteristics, such as threshold energy and intermediate species across a pseudo-binary alloy series, we explore the transition from covalent to metavalent bonding. This analysis sheds light on bonding behaviors previously linked with phase-change materials and thermoelectrics, providing a framework to inspire future research in this domain.

Experimental details

Materials. Bismuth selenide (Bi_2Se_3, 99.995%, Alfa Aesar), antimony selenide (Sb_2Se_3, 99.999%, Alfa Aesar), germanium selenide (GeSe,99.999%, American Elements), antimony (Sb, 100 mesh, 99.5+%, Sigma Aldrich), Sulfur (S, 99.5+%, Acros Organics), Ethanedithiol (EDT, Alfa Aesar), Ethylenediamine (en, Acros Organics). Fluorine-doped tin oxide (FTO) glass of 8–10 Ω sq^{-1} sheet resistance was purchased from XOP Glasses. Nitrogen and Argon flows were used in ultra-high purity (UHP) grade (99.999%). All chemicals were used as received without any further purification.

Preparation of Sb_2Se_3 and $(Bi_xSb_{1-x})_2Se_3$ thin films.

Bi_2Se_3 and Sb_2Se_3 powders (total mass of 160 mg) with various concentration ratios were gently ground with an Agar mortar and pestle for 1–2 min in air, each powder mixture was prepared individually. The powder mixtures were then transferred to a glass vial and mixed with a vortex mixer for 1 min to form a homogenous source material. After that, powder mixtures with different concentrations were added to the individual pockets of graphite source plate. After all the source materials were placed in the graphite source plate, it was loaded to the close-spaced sublimation (CSS) system and kept under high vacuum (~10^{-6} mbar) overnight. A ceramic spacer was placed in between the graphite source and top plate and the distance between source to FTO substrate was kept 10 mm. Bi_2Se_3–Sb_2Se_3 powder was heated to 575 ℃ and 590 ℃ with a ramp rate of 5 ℃ s^{-1}. After holding at the set point temperature for 3 to 4 minutes, the lamp power was switched off, and the system was allowed to cool naturally. During the deposition process, the chamber pressure was ~10^{-2} mbar and substrate temperature were 465–500 ℃ and 465-530 ℃ for a source temperature of 575 ℃ and 590 ℃, respectively. During the film deposition, the substrate remains hot enough which causes the Se re-evaporation from the film, leading to a higher Se deficiency closer to the substrate. As the film continues to grow, this effect is suppressed, and Se deficiency is reduced.

Deposition of Sb_2S_3 and $(Bi_xSb_{1-x})_2S_3$

We prepared Sb-S ink by dissolving 1.65 mmol (201.8 mg) Sb powder and 2.48 mmol (79.4 mg) S powder in 2.64 mL of ethylenediamine (en) and 6.6 mL of ethanedithiol (EDT) in a N_2-filled glovebox.[41] Similarly, $(Bi_xSb_{1-x})_2S_3$ samples were prepared by varying the Sb and Bi_2O_3 concentrations, keeping the en, EDT, and S concentrations unchanged in the solutions. To achieve x = 0.25, 0.5, and 0.75 compositions, 151.4, 50.5, and 10.1 mg of Sb, and 96.5, 289.2, and 366 mg of Bi_2O_3 were used, respectively. All the solutions were stirred at 65 ℃ for 2 hours for complete dissolution and were filtered with a 220 nm PTFE syringe filter before spin-coating at 3000 RPM for 30 s. The spin-coated

samples were then annealed at 300 ℃ under the N_2 environment for 10 min with a ramp rate of 3.33 ℃/min.

Preparation of SnS and PbS thin films. Thin films of orthorhombic and cubic SnS were prepared as described by Noy et al.[42] Similarly, the PbS thin films were deposited using a chemical deposition method.[43]

X-Ray Diffraction. Structural information (crystal phase and crystallinity) of as-deposited films were examined by using a X-ray diffractometer (PANalytical multi-purpose Empyrean II) with Cu $K_{\alpha1}$ (λ = 1.54 Å) radiation source with the X'celerator position sensitive detector. The diffractograms were collected at 40 kV voltage and 30 mA current, using a scan rate of 3° per min.

Scanning Electron Microscopy. The morphology, compactness, and EDS (energy dispersive spectroscopy) of the thin films were studied by Verios XHR 460L scanning electron microscope (SEM) equipped with an EDS detector for the compositional analysis. Accelerating voltages of 5 kV and 10 kV were used for imaging and compositional analysis, respectively.

Raman Spectroscopy. Raman spectroscopic measurements were carried out using a confocal Raman (Horiba LabRam HR Evolution). Raman spectra were recorded by using a 532 nm laser, 100 µm confocal microscopic hole, 600 grooves mm^{-1} grating, and a 50× objective lens. A Si reference Raman peak positioned at 520.5 cm^{-1} was used for calibration and all the spectra were collected from 60 to 500 cm^{-1} with an acquisition time of 60 s.

Transmission Electron Microscopy. Scanning transmission electron microscopy (STEM) studies were done with a Thermo Fisher Scientific Spectra 200, using an accelerating voltage of 200 kV with high-angle annular dark-field (HAADF) detector. EDS data was obtained with a Super-X detector. To perform an in-depth composition analysis, a cross-section of a sample in a FTO/SnO_2/$(Bi_xSb_{1-x})_2Se_3$/Au configuration with 42% Bi concentration was prepared with a dual beam focussed ion beam (FIB) and examined using a HRTEM equipped with EDS detector on a Helios G4 UC system. The cross-section was polished with 30 kV voltage and 0.9 nA current, and afterwards, 5 kV voltage and 40 pA current were used. TEM lamella was cleaned by oxygen/nitrogen plasma.

X-Ray Photoelectron Spectroscopy. X-ray photoelectron spectroscopy (XPS) was carried out in a Thermo Scientific ESCALAB 250 in an ultra-high vacuum chamber employing an Al Kα excitation source, and a 650 µm spot size. The samples were etched by Ar clusters (6 keV energy with a cluster size of 500) for 60 s to remove the surface oxygen and spectra were collected before and after etching. All core level peaks were adjusted with respect to C 1s (by taking C1s peak at 284.8 eV), and CasaXPS software was employed to analyse the results.

Computational details

Density functional theory calculations using plane wave basis sets were done using the Quantum Espresso program package.[44] We employed Projector Augmented Wave (PAW) type pseudopotentials and PBESol functional.[45,46] The required pseudopotentials were obtained from the Materials Cloud.[47] Kinetic energy cut-off greater than the minimum recommended value was chosen, and the charge density cut-off was set to four times the kinetic energy cut-off. The projected density of states (PDOS) calculations were performed with a k-spacing of 0.15 $Å^{-1}$; gaussian smearing with a degauss value of 0.005 was employed. The k-path selection for band structure calculations were done using the Xcrysden software.[48] Band structure and PDOS calculations were also done by incorporating the spin-orbit coupling effects. Grimme's D3 dispersion correction is used in all the calculations.[49] The convergence thresholds for SCF, total energy (for ionic minimization) and force are set as 1.0E-06, 1.0E-04, and 1.0E-03, respectively. Projected Crystal Orbital Hamilton Population (pCOHP) analysis to analyse the nature of interactions around the Fermi level, is performed using the program LOBSTER.[50,51]

Results

Bi_2Se_3–Sb_2Se_3 pseudo-binary alloy homologs are expected to undergo a transition from covalent to metavalent bonding with increasing Bi content.[52–54] Bi-alloying in the $(Bi, Sb)_2Ch_3$ with an orthorhombic stibnite crystal structure (Fig. 1) is feasible up to Bi/Sb = 1 for $(Bi, Sb)_2Se_3$ and throughout the full composition range for $(Bi, Sb)_2S_3$. Furthermore, according to previous studies, Bi atoms preferentially substitute the Sb at the Sb1 site in $(Bi, Sb)_2Se_3$ lattice.[55]

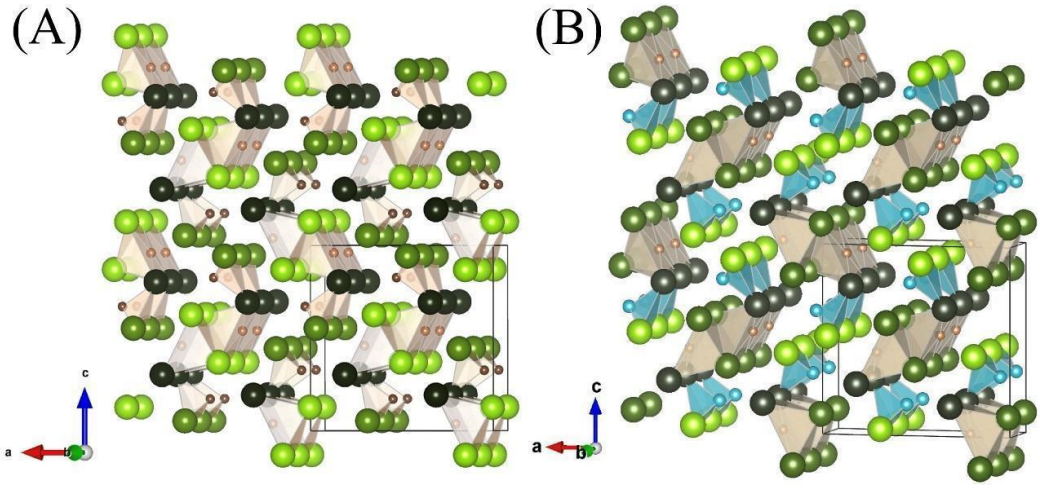

Figure 1. Crystal structure of Sb_2Se_3 and Bi-alloyed antimony selenide, $(Bi_xSb_{1-x})_2Se_3$. (A) In Sb_2Se_3 structure, brown spheres are assigned to Sb, and green spheres are assigned to Se atoms. The dark and light brown spheres are indicating Sb1 and Sb2 sites. Three Se sites are depicted by three shades of green colour. (B) In $(Bi_xSb_{1-x})_2Se_3$ structure, substituted blue spheres are corresponding to the Bi atoms in the lattice. Bi atoms preferentially go to the Sb1 site in Sb_2Se_3 lattice.[56]

Deposition of $(Bi_xSb_{1-x})_2Se_3$ thin films with 0 < x <0.42. We fabricated the Bi alloyed antimony selenide thin films using CSS and examined the films' structure, morphology, and composition using X-ray diffraction (XRD), SEM-EDS, XPS, and cross-section TEM. The morphology of as-deposited films can be inferred from the SEM images in Fig. 2. Thin films, up to ~500 nm thick, with apparent grain size of 80-320 nm were deposited. Increasing the Bi_2Se_3/Sb_2Se_3 ratio in the CSS source powder resulted in a smaller average grain size (Figs. 2D and S1), which is understandable as Bi-alloys melt at a higher temperature than antimony selenide. Therefore, grain growth occurs at higher temperature.[57,58] The lower vapor pressure of Bi_2Se_3 required a temperature of 590°C instead of 570°C in order to deposit films with Bi content $0.19 < x \leq 0.42$. Consequently, these films had a larger average grain size due to higher substrate temperature. XPS, SEM-EDS, and TEM-EDS data discussed later confirm that increasing the Bi_2Se_3/Sb_2Se_3 ratio in the source powder indeed resulted in a higher Bi content in the

deposited films, and that the metal/chalcogenide ratio is slightly Se deficient or close to stoichiometric value and is within a 1.43 < y < 1.5 range in all the films we studied.

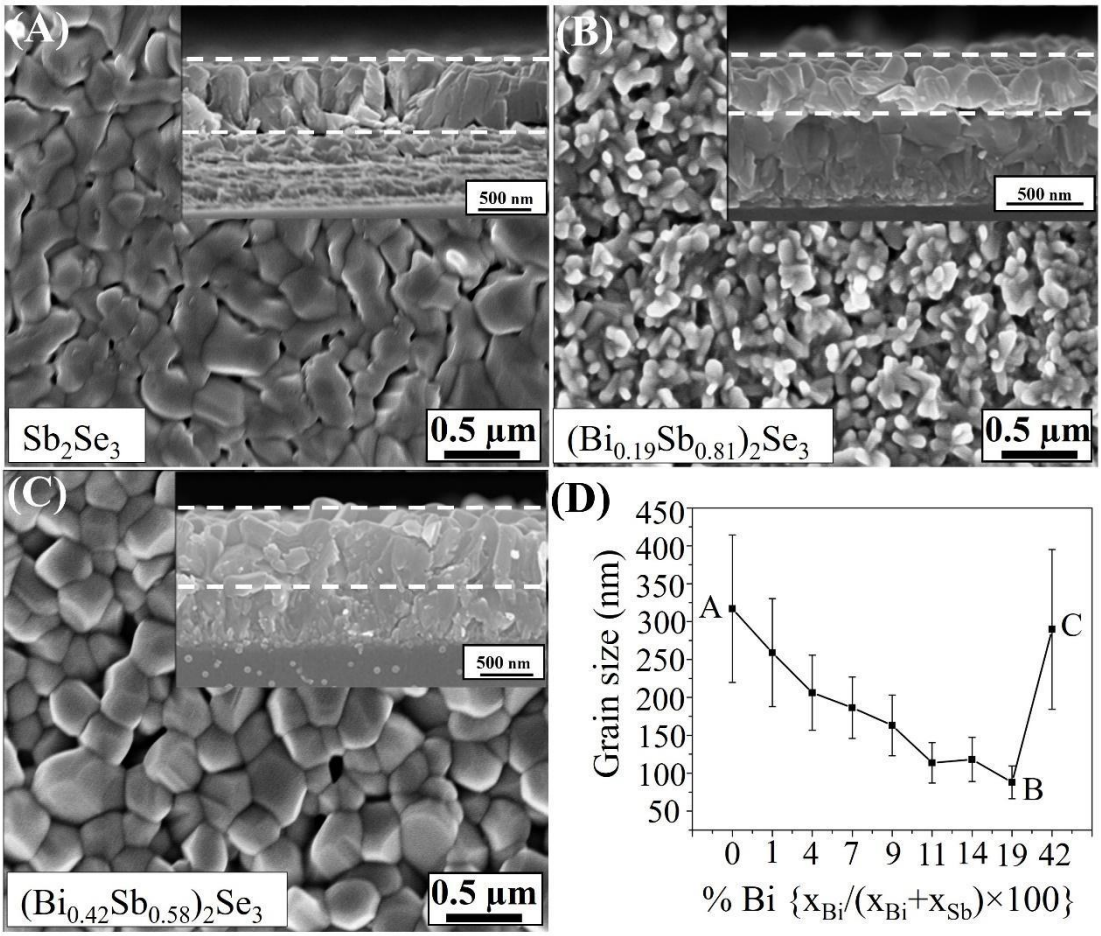

Figure 2. Scanning electron microscopy (SEM) images of bismuth-alloyed antimony selenide thin films. Cross-sections of the films are shown in the insets. Films shown in (A) and (B) were deposited at 575 °C temperature, whereas film in (C) was deposited at 590 °C. Films' thickness are shown by dashed white lines in cross-section images (inset). (D) Grain size was calculated from SEM images by using ImageJ software. The average grain size was calculated by sampling 120 grains from each sample.

Wide-angle XRD of the thin films (Fig. 3A) confirms that the orthorhombic crystal structure is maintained throughout the compositional space investigated, and it matches the powder diffraction pattern of Sb_2Se_3 (ICSD ref no. 194836). In the deposited films, we did not find evidence of secondary phases such as metal oxides or Bi_2Se_3. Selected area electron diffraction (SAED) pattern (Fig. 4D) of film with x = 0.42 depicts that the grains making up the film are highly crystalline and the phase matches that of orthorhombic Sb_2Se_3, in agreement with the XRD results. Furthermore, comparing the diffractograms of the various Bi-alloyed films (Fig. 3A), we observed a shift with higher Bi content towards lower 2θ values in reflections from (hk1) planes, such as (221) and (301) (Fig. 3B). This is

consistent with Bi substitution of the smaller Sb ions. Notably, we did not observe any noticeable shifts in reflections from (hk0) planes, such as (020) and (120) (Fig. 3C). Kyono and Kimata[59] studied the Bi-alloying in the $(Bi,Sb)_2S_3$, which has an orthorhombic crystal structure similar to Sb_2Se_3. They suggested that the larger volume of the Sb1 is a favorable site for Bi_{Sb} substitution since it has a larger coordination polyhedron than that of the Sb2 site in the $(Bi,Sb)_2S_3$.

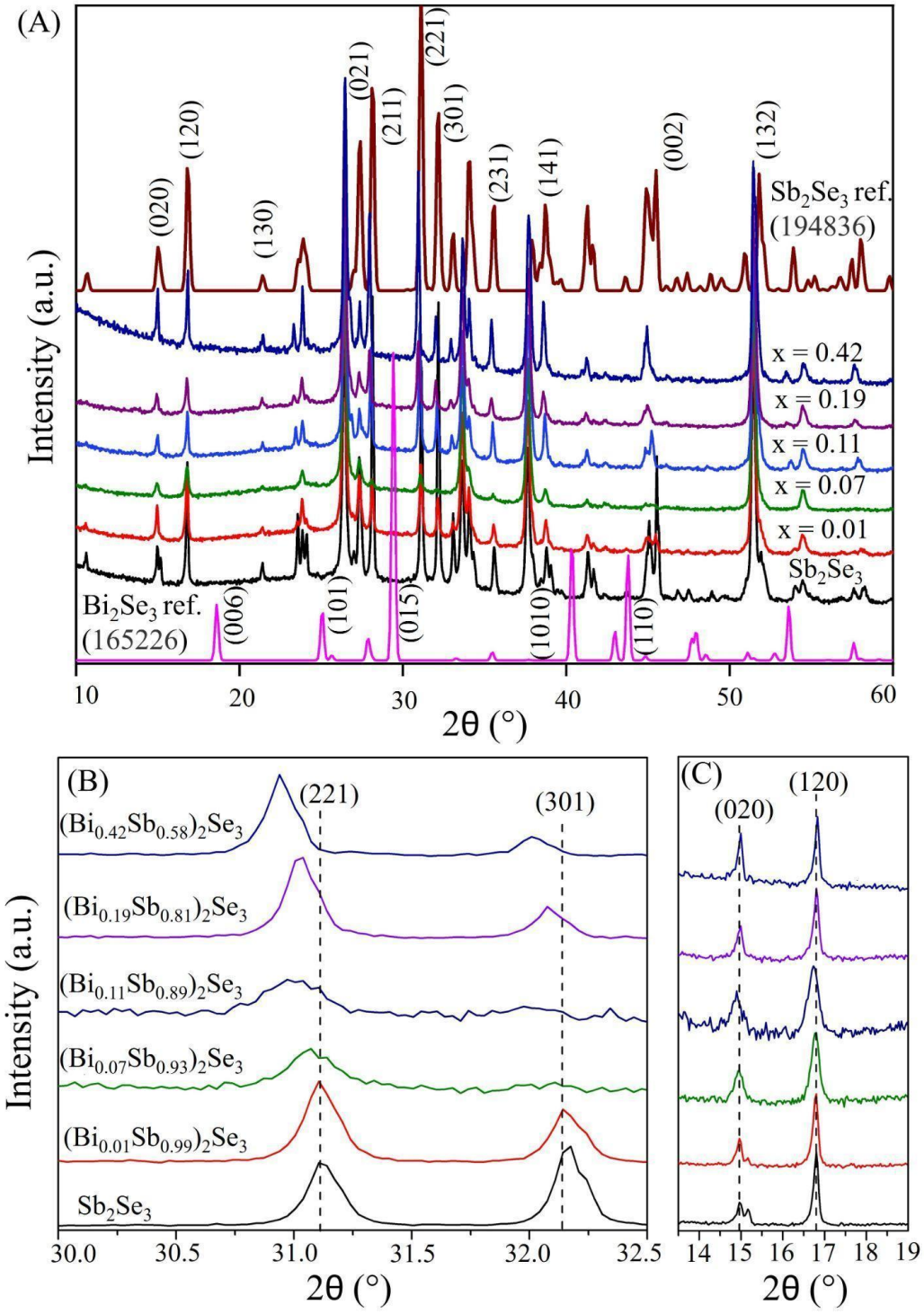

Figure 3. X-ray diffractograms of thin films of Bi-alloyed antimony selenide thin films with various Bi concentrations (x = 0, 0.01, 0.07, 0.11, 0.19, and 0.42). (A) A wide 2-theta scan showing the match between the diffraction pattern of the thin films with that of powder diffraction of antimony selenide (ICSD card no. 194836). No peaks associated with Bi_2Se_3 (ICSD card no. 165226) can be found. (B) A magnification of the 30.0-32.5 2θ range. The reflections from (221) and (301) planes shift to smaller angles, in agreement with the substitution of Sb by the larger Bi ion. (C) A magnification of the 14.0-19.0 2θ range showing that the (020) and (120) planes did not shift upon Bi_{Sb} substitution.

Next, we discuss the film composition and homogeneity. SEM-EDS results show that the thin films are slightly Se deficient or stoichiometric with Se/(Bi+Sb) ratio of 1.44-1.5, regardless of Bi content, which is in agreement with XPS analysis after short Ar-cluster cleaning (prior to cleaning, the top surface showed oxygen content of 5-6% while oxygen content redacted to 1-2% after cleaning; Table S1-2 and Figs. S2-4). XPS analysis revealed that the Bi/(Bi+Sb) ratios match the SEM-EDS analysis after cleaning. Before cleaning, the top surface had lower Bi/(Bi+Sb) ratios. For example, the $Bi/(Bi+Sb)_{after}$ was 0.11 ± 0.01 and $Bi/(Bi+Sb)_{before}$ was 0.06 ± 0.03, and in a film with a higher Bi content, $Bi/(Bi+Sb)_{after}$ was 0.42 ± 0.01, while $Bi/(Bi+Sb)_{before}$ was 0.31 ± 0.03. We also performed a nanoscale compositional analysis at three different locations within the film (marked in Fig. 4A) using STEM-EDX of cross-sections of the film. Namely, we studied the composition (a) close to the substrate, (b) near the center of the film, and (c) close to the top surface. We found that the films were consistently slightly Se deficient, and that the Se content slightly increases towards the top surface [at (a) Se/(Bi+Sb) = 1.43; at (b) and (c) Se/(Bi+Sb) = 1.47]. Bi/(Bi+Sb) ratio was similar in all locations and matched the values of SEM-EDS and XPS for the same films. Lastly, we examined the near grain boundary region, which revealed a near-homogeneous elemental distribution across the grain boundary without evidence of amorphization or phase segregation.

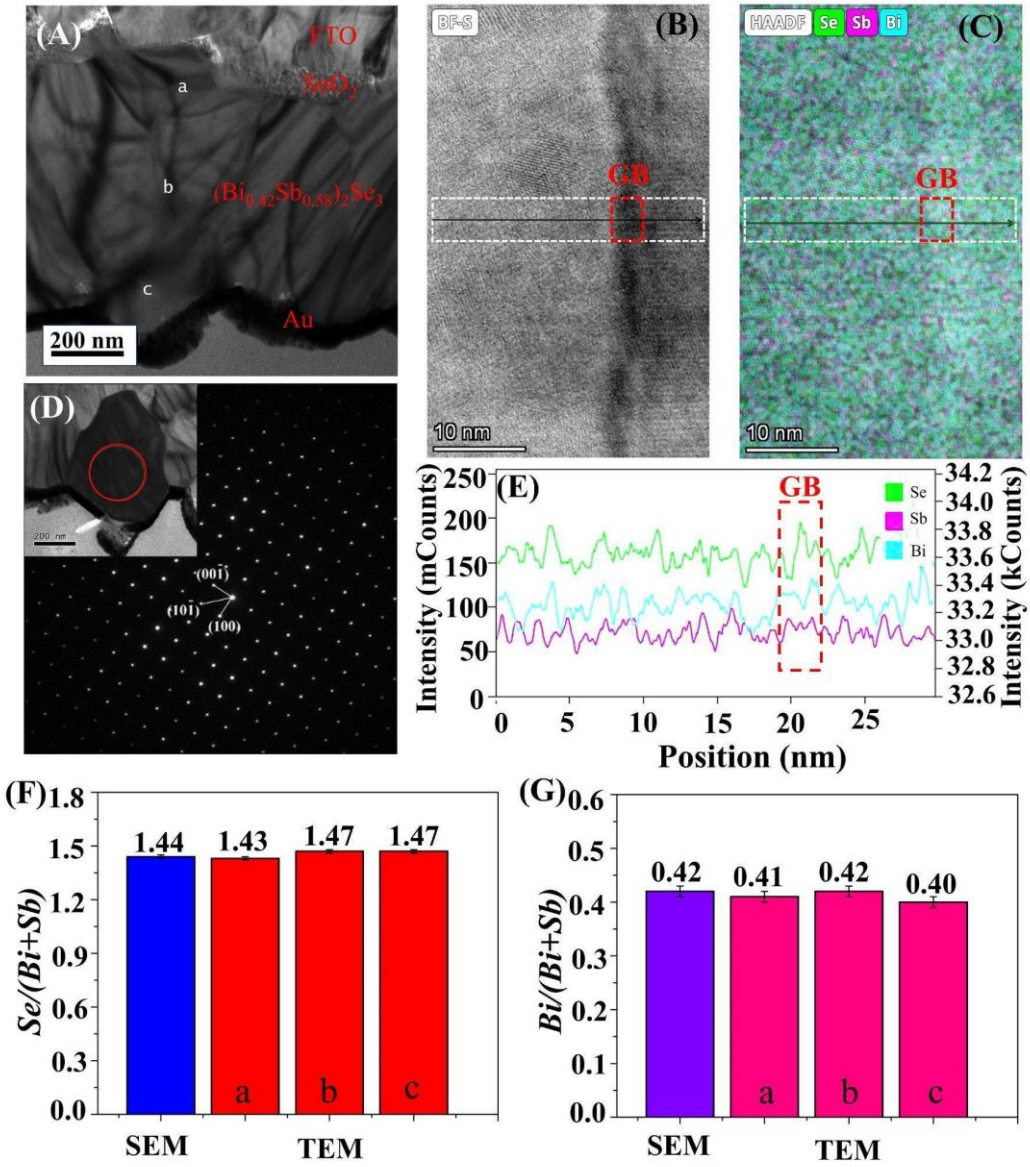

Figure 4. Transmission Electron Microscopy. (A) Low-magnification image of 42% Bi-alloyed antimony selenide thin film. The deposition direction is shown by a white arrow, and the locations where elemental analysis is performed are labeled as a, b, and c. (B) High-angle annular dark field (HAADF) image of a cross-section of a $(Bi_xSb_{1-x})_2Se_3$ with x = 0.42 at a grain boundary. (C) In the EDS elemental mapping of Bi, Sb, and Se, the region of interest is marked by a white dashed rectangle. (D) The selected area electron diffraction (SAED) pattern of the single grain (shown in the inset) is depicted. (E) Line profile of the net EDS counts signals of Sb, Bi, and Se, taken from the region indicated in (B), across the grain boundary. (F) and (G) Elemental composition of $(Bi_xSb_{1-x})_2Se_3$ with x = 0.42 measured by SEM and TEM at locations a, b, and c.

The Raman spectrum of a Sb_2Se_3 thin film (Fig. 5) shows five main peaks at 98, 128, 151, 190, and 210 cm^{-1}. The most prominent peak is evident at 190 cm^{-1} and corresponds to Sb-Se vibrations, while the

peaks at 98, 128, and 210 cm^{-1} relate to Se-Se vibrations, and the peak at 151 cm^{-1} is due to Sb-Sb vibrations. [60–63]

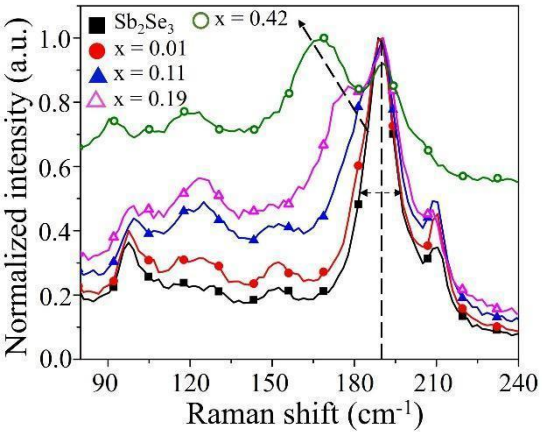

Figure 5. Raman spectra of bismuth-alloyed antimony selenide with different Bi concentrations, x = 0, 0.01, 0.11, 0.19, and 0.42. A dashed arrow shows the shoulder peak's emergence and shifting at ~176 cm^{-1}. The width of the peak ~190 cm^{-1} increases with the Bi concentration in the films. All the spectra are collected with 0.36 mW laser intensity using a 532 nm excitation wavelength.

After Bi incorporation in the antimony selenide films, we observe a shoulder peak emerging near 176 cm^{-1}, corresponding to Bi-Se vibrations.[55,64,65] This peak shifts to a lower frequency as Bi concentration increases. The shift towards lower frequency occurs since the vibrational frequency is inversely proportional to the reduced mass. Therefore, a higher mass will shift the vibrational frequency to smaller values.[55] In addition, the intensity of 151 cm^{-1} fades with Bi concentration increase. The decrease in 151 cm^{-1} peak intensity is due to Bi substitution at Sb sites.

The results thus far indicate that the $(Bi_xSb_{1-x})_2Se_3$ alloy films we deposited using CSS have high crystalline quality without evident sub-phases, impurities, or significant deviations from stoichiometry. Also, all the films maintain the orthorhombic stibnite structure regardless of composition.

Photo-induced phase transition in Sb_2Se_3 thin films. In previous studies, we discovered that SbChI and Sb_2Ch_3 undergo reversible solid-state photoreactions when excited near the bandgap with a laser exceeding a specific power threshold. These reactions transiently produce metallic antimony clusters, which dissipate after less than two hours under dark, inert conditions at 25°C, enabling the materials to self-heal and restore their original crystal structure. Spectroscopically, this process is marked by the emergence of two prominent Raman peaks at 112 and 150 cm^{-1} in Sb_2Se_3, indicating the formation of metallic Sb (Fig. S8 A), as depicted in the 'after' spectrum (Fig. 6A), alongside a reduction in the 190

cm^{-1} peak (without a peak at 250 cm^{-1} for elemental selenium or antimony oxides detected). After waiting 120 minutes in the dark, the Raman spectrum reverts to its initial state. We proposed that the photoinduced reaction in these materials is facilitated by a high density of Sb-Sb bonding states at the bottom of the conduction band. Intense light populates these states with electrons, resulting in the formation of metallic Sb clusters. After a dark period, the electrons return to their ground state, which depletes these states. We related these reactions to photoinduced phase transition (PIPT). The proposed reaction that takes place in Sb_2Se_3 is:

$$Sb_2Se_3 \rightarrow Sb_{2-x}Se_{3-y} + xSb + ySe$$

Conversely, Bi_2Se_3 shows no photoreactivity, maintaining its spectral profile unchanged even when subjected to a laser intensity five times greater (Fig. 6B).

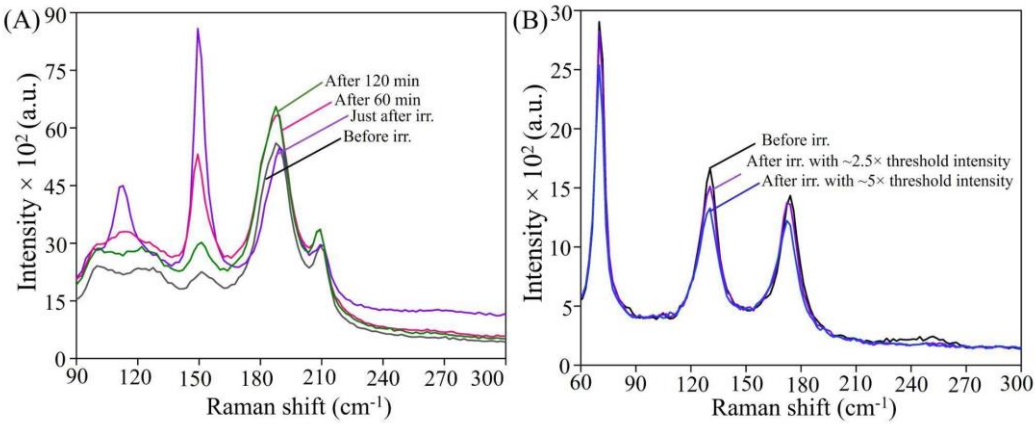

Figure 6. (A) Raman spectra illustrating the recovery of Sb_2Se_3 after irradiation. In the case of Sb_2Se_3, we used ~3.63 mW for PIPT and recorded the 'before' and 'after' spectra with 0.36 mW laser intensity. (B) Raman spectra of Bi_2Se_3 after x2.5 and x5 times higher laser power than that used for causing PIPT in Sb_2Se_3. It is evident that irrespective of the laser intensity we used, no PIPT was observed.

Substituting Bi for Sb and repeating the irradiation-collection measurements with films containing gradually increasing Bi content, we found that the prominent peaks associated with metallic Sb, especially the peak at 150 cm^{-1}, gradually diminished with increasing Bi concentration (Figs. 7B–E), becoming indistinguishable at x = 0.19. Also, as before, no oxide-related peaks were observed in any of the films regardless of the Bi content. The gradual decrease in the area of the 150 cm^{-1} peak with an increase in Bi concentration is summarized in Fig. 7F. We have also examined the effect of various parameters such as temperature, excitation wavelength, and laser intensities to check the PIPT in Bi-alloyed films. Considering that perhaps the recovery is accelerated with alloying, we recorded the Raman of alloyed films at -20°C temperature to slow the recovery (in accord with our previous findings) and probe if any photo-induced species exists at lower temperatures which are not

observable at room temperature (Fig. S8 B). We could not notice any change in the spectrum after irradiation even at -20° C temperature (Figs. S5 A and B). We also tested higher laser intensities to examine whether Bi-alloyed films require higher threshold to undergo PIPT. Nonetheless, Bi-alloyed films (x = 0.42) did not exhibit any PIPT even at higher intensities (Fig. S6 A). We also did not observe PIPT with 633 nm laser in alloyed films and Raman spectra remained intact after the irradiation (Fig. S7). However, we noticed a photo-induced phase separation (in air) when a 785 nm laser was used. Due to this phase separation, two Raman peaks at 71 and 128 cm^{-1} emerge after irradiating the films with 1.28 mW laser intensity (Fig. S6 B). Finally, for comparison, the spectra of Sb and Bi particles (99.99%, as received) under similar conditions are shown in Figure S8. None of the films, under any circumstances, have shown peaks that can be associated with metallic Bi.

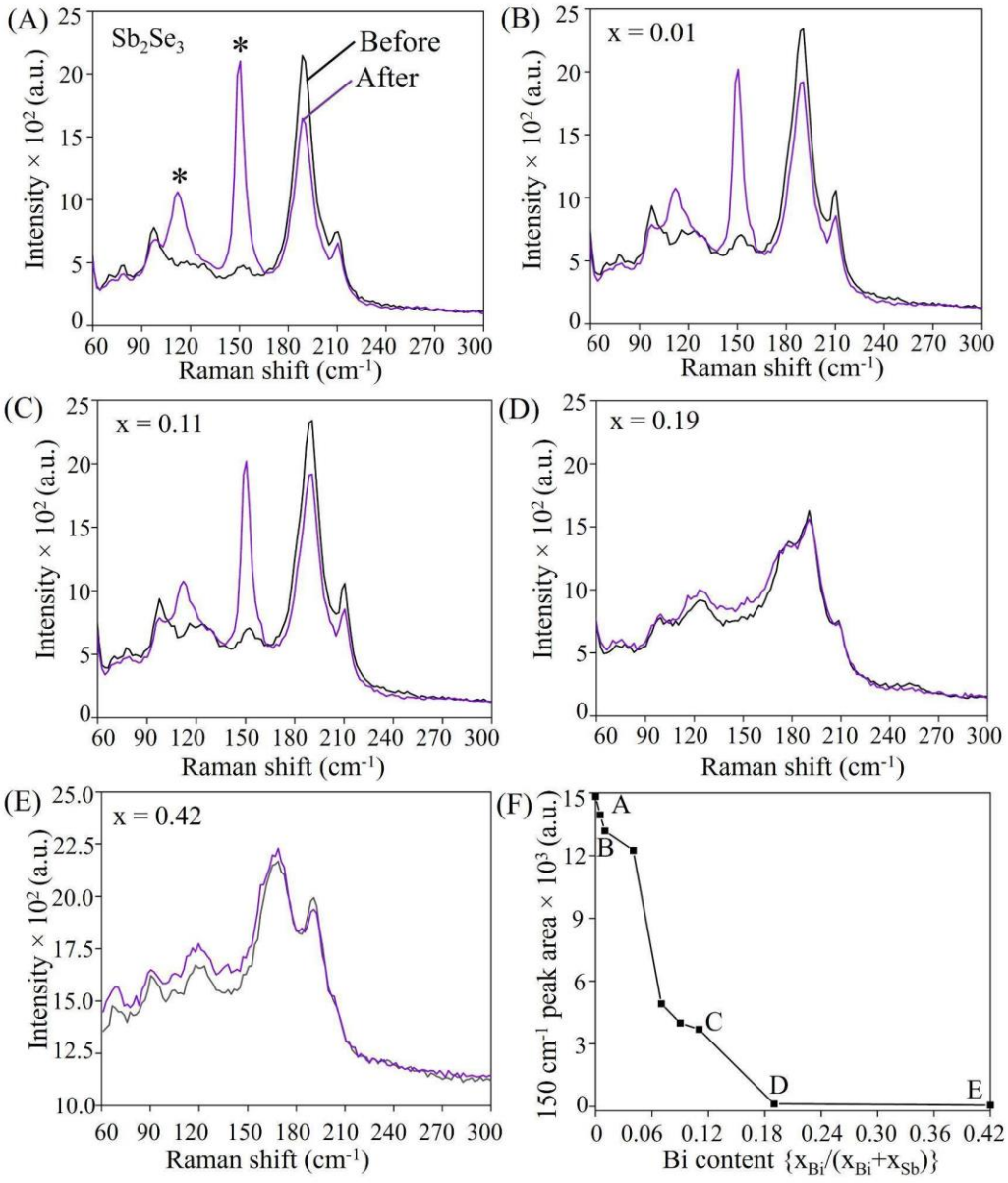

Figure 7. Raman spectra of bismuth-alloyed antimony selenide thin films. (A)-(E) The black-colored spectra were recorded by irradiating low-intensity laser 'before' PIPT and the violet spectra were collected at low-intensity 'after' PIPT. The threshold power (for antimony selenide) for PIPT was 3.63 mW. The asterisk (*) labeled peaks are the main peaks that emerge during PIPT. (F) The effect of Bi-alloying on PIPT is shown. The decrease in 150 cm^{-1} Sb Raman peak is shown with the increase in Bi-content in the alloyed films.

Therefore, along the homologous series we find an apparent 'border' in PIPT occurrence at nearly 20% of Bi content, which coincides with a gradual transition from a more covalent to a more metavalent chemical bonding. When there is a higher tendency towards a metavalent bonding, there is less tendency to undergo PIPT. We tested another material well within the 'metavalent zone' to examine this trend further.[54] Indeed, the Raman spectrum of PbS shows characteristic peaks at 200 and 451 cm^{-1} (Fig. S9), but it showed no change in the spectrum after intense irradiation, indicating the absence of PIPT in PbS film.[66,67] This result further supports the notion that metavalently bonded materials are less susceptible to this kind of PIPT. Similarly, GeSe and SnS were studied to examine the PIPT in this class of materials. In the Raman spectra of GeSe (Fig. S10 A), we observed two new peaks (~170 and 300 cm^{-1}) along with the characteristic GeSe peaks when a relatively high laser intensity (9.07 mW) was used. The peak at 300 cm^{-1} is related to the Ge-Ge vibrations which might be related to the photo and/or temperature induced phase transitions.[68,69] Afterwards, we followed the self-recovery within ~2 h and noticed that the material showed partial recovery (Fig. S10 B). Contrary to GeSe, SnS did not show any phase transformation[70–73] even after the highest laser intensity (36.3 mW) as shown in Fig. S11. A homologous series of Bi_2S_3-Sb_2S_3 was also tested for PIPT (Fig. S12). It showed PIPT with smaller (x = 0.25) Bi concentration, but as Bi concentration increased to x = 0.5 and above, there was no PIPT detected.

To shed more light on the possible relation of chemical bonding and PIPT/self-healing and extend the hypothesis on the occurrence of bonding states at the bottom of the conduction band as a PIPT-facilitating property, we calculated the projected density of states (PDOS) for Sb_2Se_3 and $BiSbSe_3$ and the crystal orbital hamilton population (-pCOHP). These are shown in Figure 8. From the PDOS of the valence band of Sb_2Se_3 we find that the majority consists of the p-orbital of Se with a minor contribution of s- and p-orbitals of Sb (Fig. 8A). Moreover, the conduction band is made of p-orbitals of Sb and Se. The positive -pCOHP values for Sb-Sb indicate bonding states near the conduction band minima (Figs. 8C and S13). Whereas the conduction band of $BiSbSe_3$ is formed from a nearly equal contribution of p-orbitals of Bi, Sb, and Se (Fig. 8B), with Sb contribution the lowest. Calculations with spin-orbit coupling gave an even lower contribution of Sb-p states in the bottom of the conduction

band (Fig. S14). The valence band is formed from the *p*-orbital of Se with a slight contribution of s and p-orbitals of Bi and Sb.

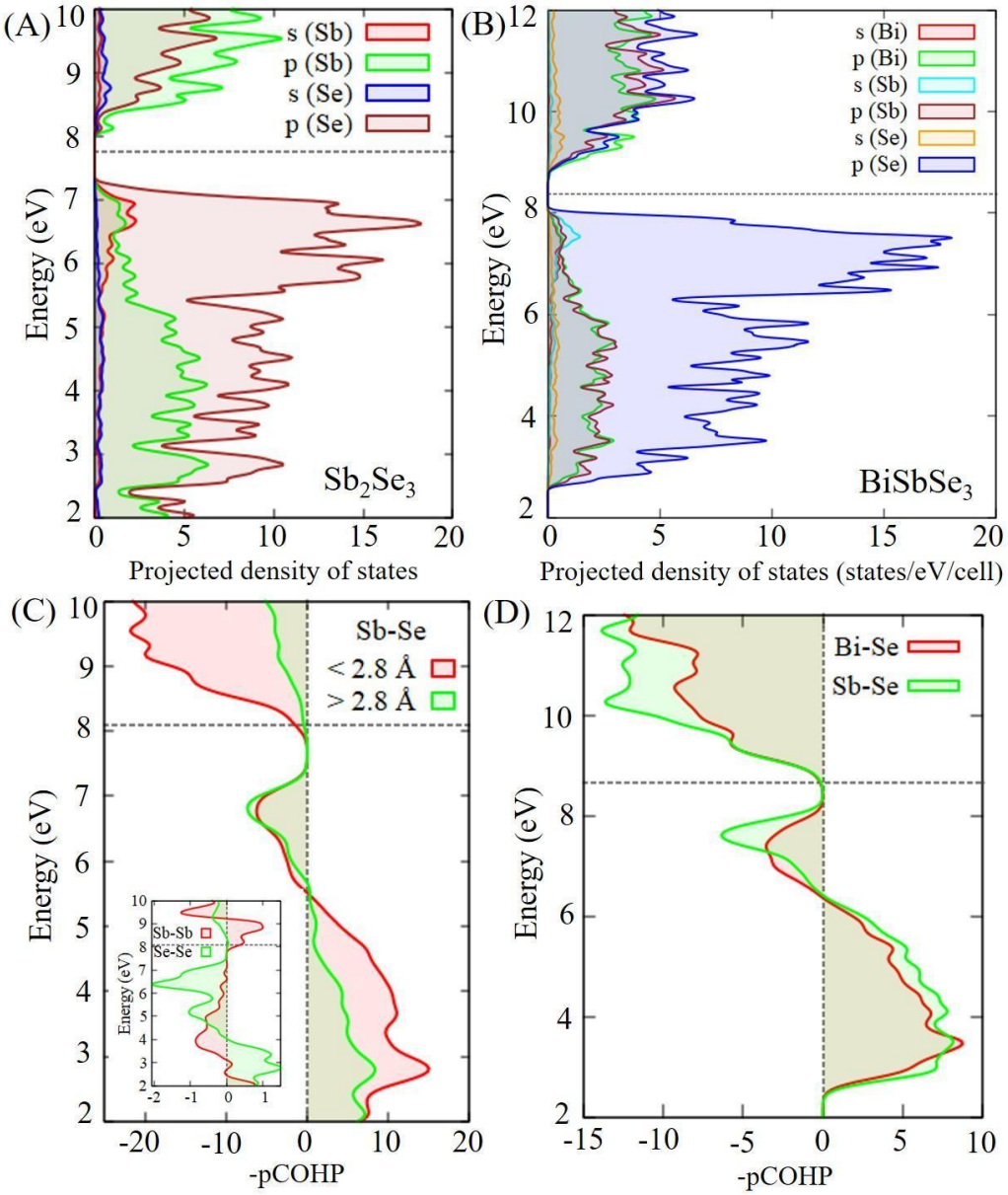

Figure 8. Projected density of states (pDOS) of (A) Sb_2Se_3 and (B) $BiSbSe_3$. The calculations are performed without the inclusion of spin-orbit coupling. Crystal Orbital Hamilton Population (COHP) figure of (C) Sb_2Se_3 and (D) $BiSbSe_3$.

Discussion

We investigated the effect of bismuth alloying on the occurrence of a photoinduced reaction in antimony selenide thin films. We deposited pristine Sb_2Se_3 and Bi-alloyed antimony selenide films by CSS and showed successful substitution of Sb by Bi up to x = 0.42 in antimony selenide without forming secondary phases and while maintaining the stibnite-like crystal structure. As we found before in Sb_2Se_3,[35] once a certain threshold laser intensity is crossed, a photoinduced reaction occurs. As a result of the reaction, metallic Sb clusters form, which after some time dissipate and the Sb_2Se_3 structure is recovered. Here we found that the photoinduced reaction gradually diminishes with an increase in Bi concentration. This is indicated by the decreasing intensity of metallic Sb peaks (112 and 150 cm^{-1}) with increasing Bi concentration (Fig. 7F). Eventually, in 19% Bi-alloyed antimony selenide the reaction was quenched, and metallic Sb peaks were not observed.

Ludovica and coworkers[52] studied the transition from covalent to metavalent bonding in Bi_2Se_3-Sb_2Se_3 system, resulting in the increase in optical dielectric constant and Born effective charge. Similarly, $Sb_2Se_{3x}Te_{3(1-x)}$ quasi-binary alloys exhibited an abrupt increase in electrical conductivity at the edge of metavalent bonding (x = ~0.63) whereas, in purely covalent bonding (x = 0), a several magnitudes lower electronic conductivity was noted. The effect of metavalent bonding on dimension reduction was probed in crystalline GeTe, which demonstrated the increase in phonon vibrations frequencies with decrease in thickness of GeTe.[53] In contrast, no such increment in Raman vibrations were noticed in amorphous GeTe. The unconventional increase with dimension reduction was attributed to enhanced electron localization as a result of metavalent bonding.

To further examine the potential correlation between metavalent bonding and the occurrence of the photoreaction, we investigated the reaction in other metal chalcogenide semiconductors labeled as 'metavalent' bonded (e.g., PbS) and 'non-metavalently' bonded (e.g., GeSe). Indeed, the PbS did not show any photoreaction, yet GeSe did. Tin disulphide (SnS_2) exhibited laser-induced phase transition from SnS_2 to SnS and Sn_2S_3.[30] Arsenic sulfide (As_2S_3) also demonstrated photo-induced phase transitions and recovery. It transforms to amorphous from crystalline phase by photo-induced amorphization after irradiation with 530.9 nm and 568.2 nm lasers.[36] Recently, halide perovskites have been explored for their photo-reactivities and self-healing properties.[10,12,14,15,19] It was shown that cesium lead bromide ($CsPbBr_3$) can self-heal after laser-induced photo-bleaching.[19] The halide perosvkites, especially the bromides, are borderline metavalent-covalent bonded semiconductors.[74] However, while it seems like there is a correlation between the bonding type and the occurrence of the photoreaction, the correlation is not straightforward. As metal chalcogenide semiconductors that are *not* metavalently bonded do *not* always show a photoreaction (e.g., SnS), and metal chalcogenide

homologous series with no expected metvalency along the tieline (Bi_2S_3-Sb_2S_3)[54] showed a diminishing photoreaction with higher bismuth content.

Our DFT analysis showed the presence of Sb-Sb bonding states at the bottom of the conduction band. Bi alloying in antimony selenide results in the incorporation of p states of Bi at the conduction band minima. As the bottom of the conduction band has lesser Sb-p states compared to Bi-p and Se-p states, the possibility of elemental antimony formation on photoexcitation also decreases. We suggest that the bonding states at the bottom of the conduction band are an additional criterion for occurrence of the photoreaction.

Conclusions

In conclusion, we studied how the Bi concentration affects PIPT in Bi-alloyed antimony selenide films deposited by CSS. We found that with the increase in Bi concentration, PIPT was gradually reduced and completely quenched at 19% concentration in alloyed films. We suggested the plausible reasons for this reduction and quenching in PIPT are the modified band structure and/or metavalent bonding in Bi-alloyed films. We deduced that along with substantial metal-metal bonding states in the conduction band, partial bonding transition from covalent to metavalent could be used to distinguish which class of materials are more likely to demonstrate PIPT.

References

(1) Py-Renaudie, A.; Soffer, Y.; Singh, P.; Kumar, S.; Ceratti, D. R.; Mualem, Y.; Rosenhek-Goldian, I.; Oron, D.; Cohen, S. R.; Schulz, P.; Cahen, D.; Guillemoles, J. F. Guided Search to Self-Healing in Semiconductors. *Adv Funct Mater* **2024**, *34* (11). DOI: 10.1002/adfm.202309107.

(2) Li, P.; Cao, K.; Gao, L.; Liao, W.; Liu, J.; Sun, X.; Wang, H.; Rao, F.; Lu, Y. Cold Welding Assisted Self-Healing of Fractured Ultrathin Au Nanowires. *Nano Express* **2020**, *1* (2). DOI: 10.1088/2632-959X/aba684.

(3) Hammood, I.; Barber, G.; Wang, B. A Review of Some of Experimental and Numerical Studies of Self-Crack-Healing in Ceramics. *International Journal of Ceramic Engineering and Science*. John Wiley and Sons Inc November 1, **2020**, pp 274–291. DOI: 10.1002/ces2.10071.

(4) Zhang, S.; van Dijk, N.; van der Zwaag, S. A Review of Self-Healing Metals: Fundamentals, Design Principles and Performance. *Acta Metallurgica Sinica (English Letters)*. Chinese Society for Metals September 1, **2020**, pp 1167–1179. DOI: 10.1007/s40195-020-01102-3.

(5) Irigoyen, M.; Matxain, J. M.; Ruipérez, F. Effect of Molecular Structure in the Chain Mobility of Dichalcogenide-Based Polymers with Self-Healing Capacity. *Polymers (Basel)* **2019**, *11* (12). DOI: 10.3390/polym11121960.

(6) van Dijk, N.; van der Zwaag, S. Self-Healing Phenomena in Metals. *Advanced Materials Interfaces*. Wiley-VCH Verlag September 7, **2018**. DOI: 10.1002/admi.201800226.

(7) Yang, Y.; Davydovich, D.; Hornat, C. C.; Liu, X.; Urban, M. W. Leaf-Inspired Self-Healing Polymers. *Chem* **2018**, *4* (8), 1928–1936. DOI: 1016/j.chempr.2018.06.001.

(8) Huynh, T. P.; Sonar, P.; Haick, H. Advanced Materials for Use in Soft Self-Healing Devices. *Advanced Materials* **2017**, *29* (19). DOI: 10.1002/adma.201604973.

(9) Irigoyen, M.; Fernández, A.; Ruiz, A.; Ruipérez, F.; Matxain, J. M. Diselenide Bonds as an Alternative to Outperform the Efficiency of Disulfides in Self-Healing Materials. *Journal of Organic Chemistry* **2019**, *84* (7), 4200–4210. DOI: 10.1021/acs.joc.9b00014.

(10) Parida, S.; Kumar, S.; Cherf, S.; Aharon, S.; Cahen, D.; Eren, B. Self-Healing and -Repair of Nanomechanical Damages in Lead Halide Perovskites. *Adv Funct Mater* **2023**, *33* (45). DOI: 10.1002/adfm.202304278.

(11) Milotti, V.; Cacovich, S.; Ceratti, D. R.; Ory, D.; Barichello, J.; Matteocci, F.; Di Carlo, A.; Sheverdyaeva, P. M.; Schulz, P.; Moras, P. Degradation and Self-Healing of FAPbBr3 Perovskite under Soft-X-Ray Irradiation. *Small Methods* **2023**, *7* (9). DOI: 10.1002/smtd.202300222.

(12) Singh, P.; Soffer, Y.; Ceratti, D. R.; Elbaum, M.; Oron, D.; Hodes, G.; Cahen, D. A-Site Cation Dependence of Self-Healing in Polycrystalline APbI3 Perovskite Films. *ACS Energy Lett* **2023**, *8* (5), 2447–2455.DOI: 10.1021/acsenergylett.3c00017.

(13) Khalfin, S.; Veber, N.; Dror, S.; Shechter, R.; Shaek, S.; Levy, S.; Kauffmann, Y.; Klinger, L.; Rabkin, E.; Bekenstein, Y. Self-Healing of Crystal Voids in Double Perovskite Nanocrystals Is Related to Surface Passivation. *Adv Funct Mater* **2022**, *32* (15). DOI: 10.1002/adfm.202110421.

(14) Ceratti, D. R.; Tenne, R.; Bartezzaghi, A.; Cremonesi, L.; Segev, L.; Kalchenko, V.; Oron, D.; Potenza, M. A. C.; Hodes, G.; Cahen, D. Self-Healing and Light-Soaking in $MAPbI_3$: The Effect of H_2O. *Advanced Materials* **2022**, *34* (35). DOI: 10.1002/adma.202110239.

(15) Finkenauer, B. P.; Akriti; Ma, K.; Dou, L. Degradation and Self-Healing in Perovskite Solar Cells. *ACS Applied Materials and Interfaces*. American Chemical Society June 1, **2022**, pp 24073–24088. DOI: 10.1021/acsami.2c01925.

(16) Nakao, W.; Osada, T.; Nishiwaki, T.; Otsuka, H. Focus on Self-Healing Materials: Recent Challenges and Innovations. *Science and Technology of Advanced Materials*. Taylor and Francis Ltd. **2021**, p 234. DOI: 10.1080/14686996.2021.1888528.

(17) Aizenshtein, B.; Etgar, L. In Situ Intrinsic Self-Healing of Low Toxic Cs2ZnX4 (X = Cl, Br) Metal Halide Nanoparticles. *Small* **2024**, *20* (2). https://doi.org/10.1002/smll.202305755.

(18) Brenner, T. M.; Egger, D. A.; Kronik, L.; Hodes, G.; Cahen, D. Hybrid Organic - Inorganic Perovskites: Low-Cost Semiconductors with Intriguing Charge-Transport Properties. *Nature Reviews Materials*. Nature Publishing Group January 11, **2016**. DOI: 10.1038/natrevmats.2015.7.

(19) Ceratti, D. R.; Cohen, A. V.; Tenne, R.; Rakita, Y.; Snarski, L.; Jasti, N. P.; Cremonesi, L.; Cohen, R.; Weitman, M.; Rosenhek-Goldian, I.; Kaplan-Ashiri, I.; Bendikov, T.; Kalchenko, V.; Elbaum, M.; Potenza, M. A. C.; Kronik, L.; Hodes, G.; Cahen, D. The Pursuit of Stability in Halide Perovskites: The Monovalent Cation and the Key for Surface and Bulk Self-Healing. *Mater Horiz* **2021**, *8* (5), 1570–1586. DOI: 10.1039/d1mh00006c.

(20) Rakita, Y.; Lubomirsky, I.; Cahen, D. When Defects Become “Dynamic”: Halide Perovskites: A New Window on Materials? *Mater Horiz* **2019**, *6* (7), 1297–1305. DOI: 10.1039/c9mh00606k.

(21) Koshihara, S. Photo-Induced Phase Transitions in Organic and Inorganic Semiconductors. *J Lumin* **2000**, *87*, 77–81. DOI: 10.1016/S0022-2313(99)00233-1.

(22) Koshihara, S.; Ishikawa, T.; Okimoto, Y.; Onda, K.; Fukaya, R.; Hada, M.; Hayashi, Y.; Ishihara, S.; Luty, T. Challenges for Developing Photo-Induced Phase Transition (PIPT) Systems: From Classical (Incoherent) to Quantum (Coherent) Control of PIPT Dynamics. *Phys Rep* **2022**, *942*, 1–61. DOI: 10.1016/j.physrep.2021.10.003.

(23) Bennemann, K. H. Photoinduced Phase Transitions. *Journal of Physics Condensed Matter* **2011**, *23* (7). DOI: 10.1088/0953-8984/23/7/073202.

(24) Cui, J.; Sun, Y.; Chen, H.; Yang, Y.; Chen, G.; Ke, P.; Nishimura, K.; Yang, Y.; Tang, C.; Jiang, N. Atomic Insights of Self-Healing in Silicon Nanowires. *Adv Funct Mater* **2023**, *33* (6). DOI: 10.1002/adfm.202210053.

(25) Fehr, M.; Schnegg, A.; Rech, B.; Astakhov, O.; Finger, F.; Bittl, R.; Teutloff, C.; Lips, K. Metastable Defect Formation at Microvoids Identified as a Source of Light-Induced Degradation in a - Si: H. *Phys Rev Lett* **2014**, *112* (6). DOI: 10.1103/PhysRevLett.112.066403.

(26) Kitagawa, R.; Takebe, H.; Morinaga, K. Photoinduced Phase Transition of Metallic SmS Thin Films by a Femtosecond Laser. *Appl Phys Lett* **2003**, *82* (21), 3641–3643. DOI: 10.1063/1.1577824.

(27) Hamanaka, H.; Tanaka, K.; Lizima, S. *Printed in Great Britain REVERSIBLE PHOTOSTRUCTURAL CHANGE iN MELT-QUENCHED As 2 S3 GLASS*; Pergamon Press, 1977; Vol. 23.

(28) Yu, Y.; Nam, G. H.; He, Q.; Wu, X. J.; Zhang, K.; Yang, Z.; Chen, J.; Ma, Q.; Zhao, M.; Liu, Z.; Ran, F. R.; Wang, X.; Li, H.; Huang, X.; Li, B.; Xiong, Q.; Zhang, Q.; Liu, Z.; Gu, L.; Du, Y.; Huang, W.; Zhang, H. High Phase-Purity 1T′-MoS2- and 1T′-MoSe2-Layered Crystals. *Nat Chem* **2018**, *10* (6), 638–643. DOI: 10.1038/s41557-018-0035-6.

(29) Akyüz, D.; Koca, A. Photo-Induced Phase Transition of CdZnS Based Nanocomposite at Room Temperature Under Solar Irradiation. *Catal Letters* **2019**, *149* (3), 876–881. DOI: 10.1007/s10562-019-02661-6.

(30) Voznyi, A.; Kosyak, V.; Onufrijevs, P.; Grase, L.; Vecstaudža, J.; Opanasyuk, A.; Medvid', A. Laser-Induced SnS2-SnS Phase Transition and Surface Modification in SnS2thin Films. *J Alloys Compd* **2016**, *688*, 130–139. DOI: 10.1016/j.jallcom.2016.07.103.

(31) Si, C.; Choe, D.; Xie, W.; Wang, H.; Sun, Z.; Bang, J.; Zhang, S. Photoinduced Vacancy Ordering and Phase Transition in MoTe2. *Nano Lett* **2019**, *19* (6), 3612–3617. DOI: 10.1021/acs.nanolett.9b00613.

(32) Ma, Y.; Liu, B.; Zhang, A.; Chen, L.; Fathi, M.; Shen, C.; Abbas, A. N.; Ge, M.; Mecklenburg, M.; Zhou, C. Reversible Semiconducting-to-Metallic Phase Transition in Chemical Vapor Deposition Grown Monolayer WSe_2 and Applications for Devices. *ACS Nano* **2015**, *9* (7), 7383–7391. DOI: 10.1021/acsnano.5b02399.

(33) Sakai, K.; Uemoto, T.; Yokoyama, H.; Fukuyama, A.; Yoshino, K.; Ikari, T.; Maeda, K. Annealing Time and Temperature Dependence for Photo-Induced Crystallization in Amorphous GeSe2. *J Non Cryst Solids* **2000**, *266-269 B*, 933–937. DOI: 10.1016/s0022-3093(00)00014-4.

(34) Griffiths, J. E.; Espinosa, G. P.; Remeika, J. P.; Phillips, J. C. *REVERSIBLE RECONSTRUCTION AND CRYSTALLIZATION OF GeSe2 GLASS*; Pergamon Press Ltd, 1981; Vol. 40.

(35) Balakrishnan, S. K.; Parambil, P. C.; Houben, L.; Asher, M.; Yaffe, O.; Edri, E. Revealing Hidden Phases and Self-Healing in Antimony Trichalcogenides and Chalcoiodides. *Cell Rep Phys Sci* **2023**, *4* (3). DOI: 10.1016/j.xcrp.2023.101298.

(36) Frumar, M.; Firth, A. P.; Owen, A. E. Optically Induced Crystal-to-Amorphous-State Transition in As2S3. *J Non Cryst Solids* **1995**, *192–193*, 447–450. DOI: 10.1016/0022-3093(95)00426-2.

(37) Ceratti, D. R.; Rakita, Y.; Cremonesi, L.; Tenne, R.; Kalchenko, V.; Elbaum, M.; Oron, D.; Potenza, M. A. C.; Hodes, G.; Cahen, D. Self-Healing Inside APbBr3 Halide Perovskite Crystals. *Advanced Materials* **2018**, *30* (10). DOI: 10.1002/adma.201706273.

(38) Duan, Z.; Liang, X.; Feng, Y.; Ma, H.; Liang, B.; Wang, Y.; Luo, S.; Wang, S.; Schropp, R. E. I.; Mai, Y.; Li, Z. Sb2Se3 Thin-Film Solar Cells Exceeding 10% Power Conversion Efficiency Enabled by Injection Vapor Deposition Technology. *Advanced Materials* **2022**, *2202969*, 1–10. DOI: 10.1002/adma.202202969.

(39) Yang, W.; Park, J.; Kwon, H. C.; Hutter, O. S.; Phillips, L. J.; Tan, J.; Lee, H.; Lee, J.; Tilley, S. D.; Major, J. D.; Moon, J. Solar Water Splitting Exceeding 10% Efficiency: Via Low-Cost Sb2Se3photocathodes Coupled with Semitransparent Perovskite Photovoltaics. *Energy Environ Sci* **2020**, *13* (11), 4362–4370. DOI: 10.1039/d0ee02959a.

(40) Chen, C.; Li, K.; Tang, J. Ten Years of Sb2Se3 Thin Film Solar Cells. *Solar RRL* **2022**, *2200094*, 1–11. DOI: 10.1002/solr.202200094.

(41) Webber, D. H.; Buckley, J. J.; Antunez, P. D.; Brutchey, R. L. Facile Dissolution of Selenium and Tellurium in a Thiol-Amine Solvent Mixture under Ambient Conditions. *Chem Sci* **2014**, *5* (6), 2498–2502. DOI: 10.1039/c4sc00749b.

(42) Zakay, N.; Mishra, N.; Maman, N.; Rashkovskiy, A.; Schlesinger, A.; Abutbul, R. E.; Ezersky, V.; Azulay, D.; Makov, G.; Golan, Y. Phase Control in Solution Deposited Tin Monosulfide Thin Films: The Role of Pb2+ Cations. *Mater Chem Front* **2023**, *7* (17), 3714–3727. DOI: 10.1039/d3qm00228d.

(43) Mishra, N.; Zakay, N.; Maman, N.; Golan, Y.; Makov, G. Epitaxial Growth of π-SnS on PbS Substrates. *Cryst Growth Des* **2023**, *23* (4), 2301–2305. DOI: 10.1021/acs.cgd.2c01332.

(44) Giannozzi, P.; Baroni, S.; Bonini, N.; Calandra, M.; Car, R.; Cavazzoni, C.; Ceresoli, D.; Chiarotti, G. L.; Cococcioni, M.; Dabo, I.; Dal Corso, A.; De Gironcoli, S.; Fabris, S.; Fratesi, G.; Gebauer, R.; Gerstmann, U.; Gougoussis, C.; Kokalj, A.; Lazzeri, M.; Martin-Samos, L.; Marzari, N.; Mauri, F.; Mazzarello, R.; Paolini, S.; Pasquarello, A.; Paulatto, L.; Sbraccia, C.; Scandolo, S.; Sclauzero, G.; Seitsonen, A. P.; Smogunov, A.; Umari, P.; Wentzcovitch, R. M. QUANTUM ESPRESSO: A Modular and Open-Source Software Project for Quantum Simulations of Materials. *Journal of Physics Condensed Matter* **2009**, *21* (39). DOI: 10.1088/0953-8984/21/39/395502.

(45) Blochl, P. E. *Projector Augmented-+rave Method*. Phys Rev B **1941**, *50*, 24.

(46) Dal Corso, A. Pseudopotentials Periodic Table: From H to Pu. *Comput Mater Sci* **2014**, *95*, 337–350. DOI: 10.1016/j.commatsci.2014.07.043.

(47) Prandini, G.; Marrazzo, A.; Castelli, I. E.; Mounet, N.; Marzari, N. Precision and Efficiency in Solid-State Pseudopotential Calculations. *NPJ Comput Mater* **2018**, *4* (1). DOI: 10.1038/s41524-018-0127-2.

(48) Kokalj, A. XCrySDen-a New Program for Displaying Crystalline Structures and Electron Densities. *J Mol Graph Model* **2000,** *17,* 176-179. DOI: 10.1016/s1093-3263(99)00028-5.

(49) Grimme, S.; Antony, J.; Ehrlich, S.; Krieg, H. A Consistent and Accurate Ab Initio Parametrization of Density Functional Dispersion Correction (DFT-D) for the 94 Elements H-Pu. *Journal of Chemical Physics* **2010**, *132* (15). DOI: 10.1063/1.3382344.

(50) Dronskowski, R.; Blochl, P. E. Crystal Orbital Hamilton Populations (COHP). Energy-Resolved Visualization of Chemical Bonding in Solids Based on Density-Functional Calculations. *J Phys Chem* **1993,** *97,* 8617-8624. DOI: 10.1021/j100135a014.

(51) Maintz, S.; Deringer, V. L.; Tchougréeff, A. L.; Dronskowski, R. LOBSTER: A Tool to Extract Chemical Bonding from Plane-Wave Based DFT. *J Comput Chem* **2016**, *37* (11), 1030–1035. DOI: 10.1002/jcc.24300.

(52) Guarneri, L.; Jakobs, S.; von Hoegen, A.; Maier, S.; Xu, M.; Zhu, M.; Wahl, S.; Teichrib, C.; Zhou, Y.; Cojocaru-Mirédin, O.; Raghuwanshi, M.; Schön, C. F.; Drögeler, M.; Stampfer, C.; Lobo, R. P. S. M.; Piarristeguy, A.; Pradel, A.; Raty, J. Y.; Wuttig, M. Metavalent Bonding in Crystalline Solids: How Does It Collapse? *Advanced Materials* **2021**, *33* (39). DOI: 10.1002/adma.202102356.

(53) Wuttig, M.; Schön, C. F.; Lötfering, J.; Golub, P.; Gatti, C.; Raty, J. Y. Revisiting the Nature of Chemical Bonding in Chalcogenides to Explain and Design Their Properties. *Advanced Materials* **2023**, *35* (20). DOI: 10.1002/adma.202208485.

(54) Cheng, Y.; Wahl, S.; Wuttig, M. Metavalent Bonding in Solids: Characteristic Representatives, Their Properties, and Design Options. *Physica Status Solidi - Rapid Research Letters* **2021**, *15* (3). DOI: 10.1002/pssr.202000482.

(55) Kumar, J.; Dror, Y.; Edri, E. $(Bi_xSb_{1-x})_2Se_3$ Thin Films for Short Wavelength Infrared Region Solar Cells. *J Mater Chem C Mater* **2022**, *10* (22), 8702–8710. DOI: 10.1039/d2tc01300b.

(56) Momma, K.; Izumi, F. VESTA 3 for Three-Dimensional Visualization of Crystal, Volumetric and Morphology Data. *J Appl Crystallogr* **2011**, *44* (6), 1272–1276. DOI: 10.1107/S0021889811038970.

(57) Chemical Bonds in Solids: X-Ray and Thermodynamic Investigations, Ed.; Springer, New York, 1972.

(58) Ghosh, G. The Sb-Se (Antimony-Selenium) System. *J Phase Equilibria* **1993**, *14*, 753–763.

(59) Kimata, A. K. M. Structural Variations Induced by Difference of the Inert Pair Effect in the Stibnite-Bismuthinite Solid Solution Series $(Sb,Bi)_2S_3$. *American Mineralogist* **2004**, *89*, 932–940. DOI: 10.2138/am-2004-0702

(60) Shongalova, A.; Correia, M. R.; Teixeira, J. P.; Leitão, J. P.; González, J. C.; Ranjbar, S.; Garud, S.; Vermang, B.; Cunha, J. M. V.; Salomé, P. M. P.; Fernandes, P. A. Growth of Sb2Se3 Thin Films by Selenization of RF Sputtered Binary Precursors. *Solar Energy Materials and Solar Cells* **2018**, *187*, 219–226. DOI: 10.1016/j.solmat.2018.08.003.

(61) Vashishtha, A.; Vana, O.; Edri, E. Nanoscale Advances Solvent Composition Regulates the Se: Sb Ratio in Antimony Selenide Nanowires Deposited from Thiol – Amine Solvent Mixtures. **2022**, *3* (001), 772–781. DOI: 10.1039/d1na00814e.

(62) Vidal-Fuentes, P.; Guc, M.; Alcobe, X.; Jawhari, T.; Placidi, M.; Pérez-Rodríguez, A.; Saucedo, E.; Roca, V. I. Multiwavelength Excitation Raman Scattering Study of Sb2Se3 Compound: Fundamental Vibrational Properties and Secondary Phases Detection. *2d Mater* **2019**, *6* (4). DOI: 10.1088/2053-1583/ab4029.

(63) Vashishtha, A.; Kumar, J.; Singh, N.; Edri, E. Surface Potential Variation across (hk1) and non-(hk1) Grain Boundaries of Antimony Triselenide. *J Alloys Compd* **2023**, *948*. DOI: 10.1016/j.jallcom.2023.169714.

(64) Gnezdilov, V.; Pashkevich, Y. G.; Berger, H.; Pomjakushina, E.; Conder, K.; Lemmens, P. Helical Fluctuations in the Raman Response of the Topological Insulator Bi2Se3. *Phys Rev B Condens Matter Mater Phys* **2011**, *84* (19), 1–5. DOI: 10.1103/PhysRevB.84.195118.

(65) Kung, H. H.; Salehi, M.; Boulares, I.; Kemper, A. F.; Koirala, N.; Brahlek, M.; Lošťák, P.; Uher, C.; Merlin, R.; Wang, X.; Cheong, S. W.; Oh, S.; Blumberg, G. Surface Vibrational Modes of the Topological Insulator Bi2Se3 Observed by Raman Spectroscopy. *Phys Rev B* **2017**, *95* (24), 1–9. DOI: 10.1103/PhysRevB.95.245406.

(66) Smith, G. D.; Firth, S.; Clark, R. J. H.; Cardona, M. First- and Second-Order Raman Spectra of Galena (PbS). *J Appl Phys* **2002**, *92* (8), 4375–4380. DOI: 10.1063/1.1505670.

(67) Bierman, M. J.; Lau, Y. K. A.; Jin, S. Hyperbranched PbS and PbSe Nanowires and the Effect of Hydrogen Gas on Their Synthesis. *Nano Lett* **2007**, *7* (9), 2907–2912. DOI: 10.1021/nl071405l.

(68) Tołłoczko, A.; Zelewski, S. J.; Błaszczak, M.; Woźniak, T.; Siudzińska, A.; Bachmatiuk, A.; Scharoch, P.; Kudrawiec, R. Optical Properties of Orthorhombic Germanium Selenide: An Anisotropic Layered Semiconductor Promising for Optoelectronic Applications. *J Mater Chem C Mater* **2021**, *9* (41), 14838–14847. DOI: 10.1039/d1tc04280g.

(69) Wang, J. J.; Zhao, Y. F.; Zheng, J. D.; Wang, X. T.; Deng, X.; Guan, Z.; Ma, R. R.; Zhong, N.; Yue, F. Y.; Wei, Z. M.; Xiang, P. H.; Duan, C. G. Strain-Engineering on GeSe: Raman Spectroscopy Study. *Physical Chemistry Chemical Physics* **2021**, *23* (47), 26997–27004. DOI: 10.1039/d1cp03721h.

(70) Chalapathi, U.; Poornaprakash, B.; Park, S. H. Chemically Deposited Cubic SnS Thin Films for Solar Cell Applications. *Solar Energy* **2016**, *139*, 238–248. DOI: 10.1016/j.solener.2016.09.046.

(71) Abutbul, R. E.; Garcia-Angelmo, A. R.; Burshtein, Z.; Nair, M. T. S.; Nair, P. K.; Golan, Y. Crystal Structure of a Large Cubic Tin Monosulfide Polymorph: An Unraveled Puzzle. *CrystEngComm* **2016**, *18* (27), 5188–5194. DOI: 10.1039/c6ce00647g.

(72) Abutbul, R. E.; Segev, E.; Zeiri, L.; Ezersky, V.; Makov, G.; Golan, Y. Synthesis and Properties of Nanocrystalline π-SnS-a New Cubic Phase of Tin Sulphide. *RSC Adv* **2016**, *6* (7), 5848–5855. DOI: 10.1039/c5ra23092f.

(73) Guc, M.; Andrade-Arvizu, J.; Ahmet, I. Y.; Oliva, F.; Placidi, M.; Alcobé, X.; Saucedo, E.; Pérez-Rodríguez, A.; Johnson, A. L.; Izquierdo-Roca, V. Structural and Vibrational Properties of α- and π-SnS Polymorphs for Photovoltaic Applications. *Acta Mater* **2020**, *183*, 1–10. DOI: 10.1016/j.actamat.2019.11.016.

(74) Wuttig, M.; Schön, C. F.; Schumacher, M.; Robertson, J.; Golub, P.; Bousquet, E.; Gatti, C.; Raty, J. Y. Halide Perovskites: Advanced Photovoltaic Materials Empowered by a Unique Bonding Mechanism. *Adv Funct Mater* **2022**, *32* (2). DOI: 10.1002/adfm.202110166.